ORIGINAL ARTICLE

Open Access

Microstructure, Corrosion and Mechanical Properties of Medium-Thick 6061-T6 Alloy/T2 Pure Cu Dissimilar Joints Produced by Double Side Friction Stir Z Shape Lap-Butt Welding

Jiuxing Tang[1], Guoxin Dai[1], Lei Shi[1*] , Chuansong Wu[1], Sergey Mironov[2], Surendra Kumar Patel[1], Song Gao[3] and Mingxiao Wu[4]

Abstract

A novel double side friction stir Z shape lap-butt welding (DS-FSZW) process was proposed to achieve excellent mechanical properties of Al/Cu medium-thick dissimilar joints. The influence of welding parameters on weld microstructure and properties of DS-FSZW joint were systematically investigated. It indicated that defect-free medium-thick Al/Cu DS-FSZW joint could be achieved under an optimal welding parameter. DS-FSZW joint was prone to form void defects in the bottom of the second-pass weld. The recrystallization mechanisms at the top and middle of the weld nugget zone (WNZ) were continuous dynamic recrystallization (CDRX) and geometric dynamic recrystallization (GDRX). While the major recrystallization mechanism at the bottom of the WNZ was GDRX. DS-FSZW joint of the optimal welding condition with 850 r/min-400 mm/min was produced with a continuous thin and crack-free IMCs layer at the Al/Cu interface, and the maximum tensile strength of this joint is 160.57 MPa, which is equivalent to 65.54% of pure Cu base material. Moreover, the corrosion resistance of Al/Cu DS-FSZW joints also achieved its maximum value at the optimal welding parameter of 850 r/min-400 mm/min. It demonstrates that the DS-FSZW process can simultaneously produce medium-thick Al/Cu joints with excellent mechanical performance and corrosion resistance.

Keywords DS-FSZW, Al/Cu dissimilar joint, Corrosion behaviour, Intermetallic compounds, Microstructure, Mechanical properties

1 Introduction

Copper (Cu) is extensively employed in the power industry for its excellent electrical conductivity but is scarce and expensive. Aluminium (Al) also has good electrical conductivity but it is cheaper than Cu. Application of Al/Cu dissimilar joints can take full advantage of Al and Cu to reduce product costs and broaden the scope of their applications, so scholars have carried out many works on Al/Cu dissimilar welding.

Some scholars have conducted experiments with Al/Cu fusion welding, Li et al. [1] used the CMT method to obtain Al/Cu butt joints, and found that two intermetallic compound (IMCs) layers were generated at the Al/Cu interface, including one IMCs layer thickness close to the

*Correspondence:
Lei Shi
lei.shi@sdu.edu.cn
[1] MOE Key Lab for Liquid-Solid Structure Evolution and Materials Processing, Shandong University, Jinan 250061, China
[2] Laboratory of Mechanical Properties of Nanoscale Materials and Superalloys, Belgorod State University, Belgorod 308015, Russia
[3] School of Mechanical Engineering, Qilu University of Technology (Shandong Academy of Sciences), Jinan 250353, China
[4] State Grid Henan Electric Power Research Institute, Zhengzhou 450052, China

Cu side with less than 5 μm and the other layer having an irregular nonlinear and zigzag shape. The joint's strength was low due to the thick IMCs layer and pores. Zhou et al. [2] used the DE-GMAW-brazing method to join 5052 Al alloy and pure Cu, the maximum shear strength was 17.66 MPa. Cai et al. [3] obtained butt joints using BA188Si filler metal by brazing 3003 Al alloy and T2 Cu, they found that interface mainly consisted of Al_4Cu_9, α-Al and (Si phases+ α-A1+ Al_2Cu) eutectic phases, and the maximum tensile strength was 56 MPa. Feng et al. [4] employed some filler metals to join 1060 Al and pure Cu, the joint's maximum shear strength was 88 MPa when using Zn-15Al filler metal. According to the above analysis, it is clear that the high temperatures of fusion welding easily form numerous IMCs and other defects, which significantly reduces the joint's mechanical properties.

Friction stir welding (FSW) has low heat input and welding temperature, which is favorable for joining dissimilar materials, such as Al and Cu [5], Al and Mg [6], Al and Ti [7], Al and steel [8]. Zhang et al. [9] analyzed the influence of the tool offset on the mechanical properties of Al/Cu joints, the results showed that the IMCs was significantly reduced when the tool was shifted 2 mm to the Al side, and the maximum tensile strength of the joint was approximately 222 MPa. Khajeh et al. [10] created the AA2024/pure Cu joint by FSW, they found that when the tool's welding speed and rotational speed were 948 r/min and 85 mm/min respectively, the joint's optimum tensile strength was 142 MPa and the elongation was approximately 5%. In the stirring zone, IMCs was formed between the Cu strip and Al, which was identified as Al_2Cu and Al_4Cu_9. Muhammad et al. [11] studied the effect of ultrasound and plate offset on 6061-T6 Al/pure Cu joint's surface appearance, electrical and mechanical properties, indicating that the weld surface roughness was reduced by ultrasound, and the maximum tensile strength of the joint was 199.57 MPa under the ultrasound application and Cu plate on the retreating side. You et al. [12] used ultrasonic dynamic-stationary shoulder FSW to join 2219-T6 Al alloy and pure Cu, they demonstrated that ultrasonic not only eliminates microcracks and reduces the interfacial IMCs layer thickness, but also reduces the residual stresses. The joint's maximum tensile strength was 247 MPa, which was 91.5% of pure Cu base material and the fracture located at the non-interface. However, the above-mentioned investigations on Al/Cu FSW were mainly focused on thin plates below 4 mm thick, while there was relatively little investigation on Al/Cu medium-thick plate FSW above 4 mm thick. Since Al/Cu medium-thick plates have a wide variety of applications in the power industry, such as transition terminal connector, switchgear, bimetallic busbar [13–15], it is necessary to study Al/Cu medium-thick

plates. Safi et al. [16] utilized the warm friction stir welding to join 5 mm thick 7075 Al alloy and pure Cu, it revealed that the joint's maximum tensile strength was 84 MPa under moderate preheating temperature conditions due to the precipitation hardening and grain refinement. Avettand-Fenoël et al. [17] fabricated the 5 mm thick 6082-T6 Al alloy/pure Cu FSW joint, an about 4 μm thick IMCs layer appeared at the interface, which identified as the Al_4Cu_9 and Al_2Cu. Muthu et al. [18] obtained a 6 mm thick AA1100-H14 Al/Cu FSW joint, the joint's maximum tensile strength and joint efficiency were 113 MPa and 70.62%, respectively. The IMCs layer thickness of the interface was about 1.9 μm with the compose of Al_2Cu, AlCu and Al_4Cu_9 phases. Mehta et al. [19] studied the effect of tilt angle on the mechanical properties of 6.3 mm thick AA6061-T6 Al/Cu FSW joints, the joint's maximum tensile strength was 117 MPa at the tilt angle of 4°, which probably attributed to large tilt angle producing the defect-free joints and good metallurgical bond between Al and Cu. Ouyang et al. [20] utilized FSW to join the 6061-T6 Al and pure Cu with a thickness of 12.7 mm, which demonstrated that the peak temperature reaching 580 °C in the weld zone near the Al side, causing abundant IMCs to appear in the joint, thus it was hard to achieve a high-quality Al/Cu connection. For the joining of medium-thick plates, conventional FSW requires a tool with a large shoulder, which probably causes the thick IMCs in the top of the workpiece and insufficient heat input to form voids and unwelded joints in the bottom of the workpiece. Thus, it is difficult to obtain high-strength joints. Therefore, double side FSW (DS-FSW) was employed for joining Al/Cu medium-thick plate, although using a tool with a small shoulder can successfully minimize welding heat input and inhibit the thickening of IMCs layer, thereby contributing to the improvement of the joint's mechanical properties. However, both welds were located along the same vertical line, when welding the second-pass weld, the first-pass weld was easily cracked, and the joint's optimal tensile strength was only 135.11 MPa [21]. To overcome this problem, a novel DS-FSZW process was introduced, which made both welds not located in the same line, and it could effectively prevent the first-pass weld from being cracked. Furthermore, the contact area of dissimilar materials was increased to avoid the weak parts of both welds being located in the same position and a butt-joint composite joint was obtained, which was beneficial for obtaining medium-thick Al/Cu joints with excellent mechanical properties [22]. However, the microstructure, corrosion behaviour and mechanical properties of Al/Cu DS-FSZW joints have not been systematically studied.

In this paper, DS-FSZW experiments were performed using the 6061-T6 Al alloy/T2 pure copper with a
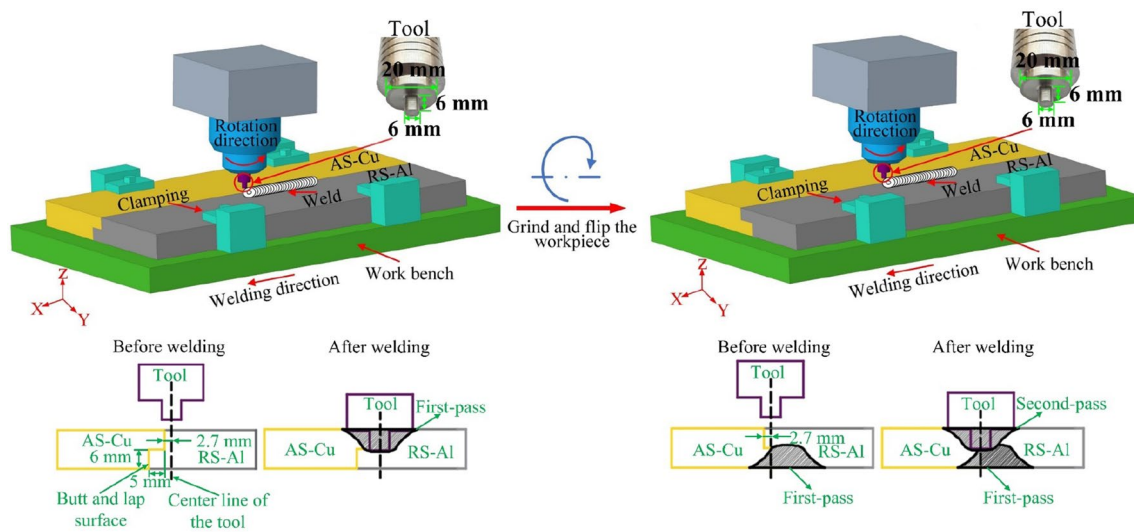
Figure 1 Schematic diagram of Al/Cu medium-thick joint produced by DS-FSZW

thickness of 12 mm, the influence of welding parameters on the microstructure and properties of Al/Cu medium-thick DS-FSZW joints were systematically investigated. It provides solid theoretical guidance and technical support for high-quality joining of Al/Cu composite structures.
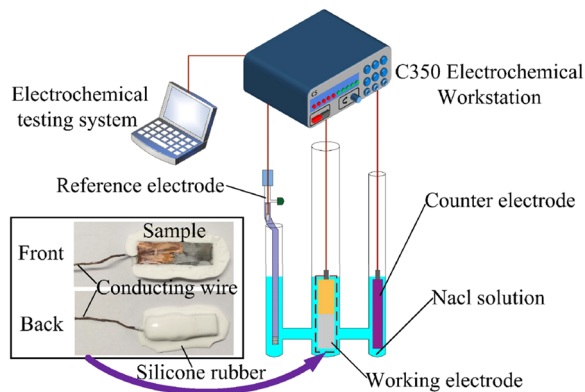
2 Experimental Procedures

The selected experiment materials were 6061-T6 Al alloy and T2 pure Cu plates with a thickness of 12 mm. In order to avoid a large number of material adhesions in the tool during the welding process and achieve high-quality Al/Cu joints, the H13 steel cylindrical tool without threads was selected, the dimensions of the tool were shown in Figure 1. Tool's tilt angle was 2.5° and plunge depth remained constant at 0.2 mm. The Cu plate was positioned on the advancing side, the tool was shifted 2.7 mm toward Al side. In this paper, the welding parameters were aliased as rotational speed and welding speed. For example, the welds were achieved at 700 r/min-100 mm/min or 700-100, which indicated the welds were produced at the rotational speed of 700 r/min with the welding speed of 100 mm/min for both side welds. The schematic diagram of the DS-FSZW process was illustrated in Figure 1, the Al and Cu were used milling machine to process into a Z shape. Before welding, the sandpaper was utilized to polish the oxide layer on the base material surface. The front side of the workpiece was firstly welded to obtain a butt joint and the flash of the first-pass weld was polished, then flip the workpiece over and join the second-pass weld on the back side of the workpiece to obtain a butt joint.

After welding was completed, using the electrical discharge machining to cut the tensile specimens, OM
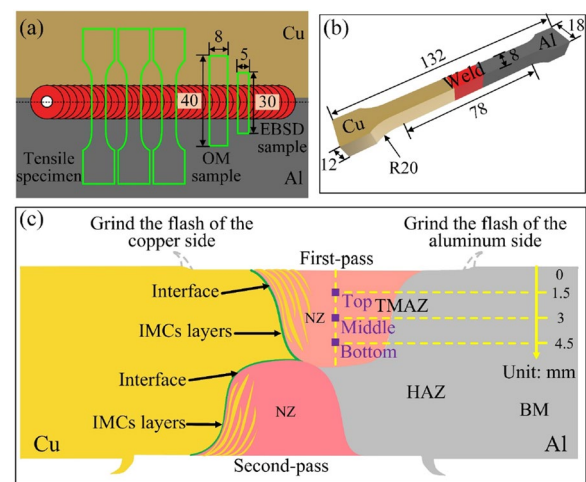
Figure 2 (**a**) Location of tensile specimens, OM sample and EBSD sample, (**b**) Size of the tensile specimen, (**c**) Location of EBSD samples

samples and EBSD samples, which were shown in Figure 2(a). The tensile sample adopted the GB/T 228.1-2010 standard, the specific dimension was shown in Figure 2(b). At least three specimens for each welding parameter were taken for tensile testing with the CMT-50 machine under a tensile rate of 1 mm/min. The final tensile strength of each welding parameter was calculated from the average tensile strength of all test samples. When the metallographic specimen has been ground and polished, a JSM-7800 F SEM equipped with EDS was utilized to analyze the interface microstructure and fracture morphologies of the joint. As for EBSD samples, after mechanical polishing, the polishing was continued by using a silica solution. When the EBSD sample was
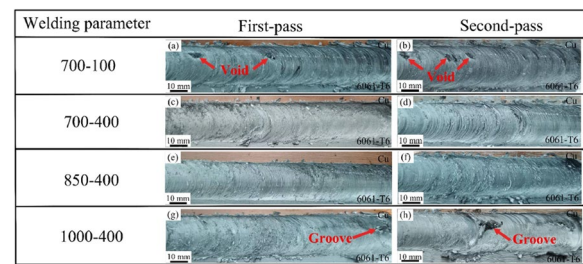
Figure 3 Electrochemical corrosion test systems

Figure 4 (a)-(h) Al/Cu weld surface at different welding parameters

Figure 5 Transverse cross-section of Al/Cu dissimilar joints under different welding parameters: (**a**) 700-100, (**b**) 700-200, (**c**) 700-300, (**d**) 700-400, (**e**) 700-500, (**f**) 600-400, (**g**) 850-400, (**h**) 1000-400

prepared, the different locations of the weld nugget zone of the first-pass weld were examined using a JSM-7800F SEM equipped with a NordlysMax3 EBSD system (Figure 2(c)) and finally the data was processed by Channel 5 software. Microhardness was tested using DHV-1000 instrument with a loading of 300 g and dwell time of 10 s.

In the electrochemical corrosion test, the saturated calomel electrode (SCE) was the reference electrode, the platinum electrode was the counter electrode, and the 3.5 wt.% NaCl solution was selected as the corrosive solution. The test surface was polished with sandpaper, then Cu wires were attached to the back of the specimen and fixed with conductive adhesive, and using silicone rubber to seal the other sides of the specimen, which means only the polished side of joint was reacted with the corrosive medium. The potentiodynamic polarization curves were tested with a scanning speed of 1 mV/s, the range of scanning potential was −0.6 to 0.6 V and the sampling frequency remained at 2 Hz during the testing. The corrosion potential and corrosion current density were fitted using Tafel to compare the electrochemical corrosion properties of the different samples. The electrochemical corrosion test system is shown in Figure 3.

3 Results and Discussion

3.1 Weld Formation

Figure 4 displays the Al/Cu weld surface at different welding parameters. When the welding heat input is high, such as 700 r/min-100 mm/min, some voids and groove defects, as well as large flashes, are formed on the weld surface. This is due to the relatively high heat input resulting in the plastic material sticking heavily to the tool, so the material cannot flow and mix well and eventually forms grooves or void defects in both welds. When a medium welding heat input is used, such as 700 r/min-400 mm/min, the weld surface is well formed with less flash because the lower heat input makes the tool
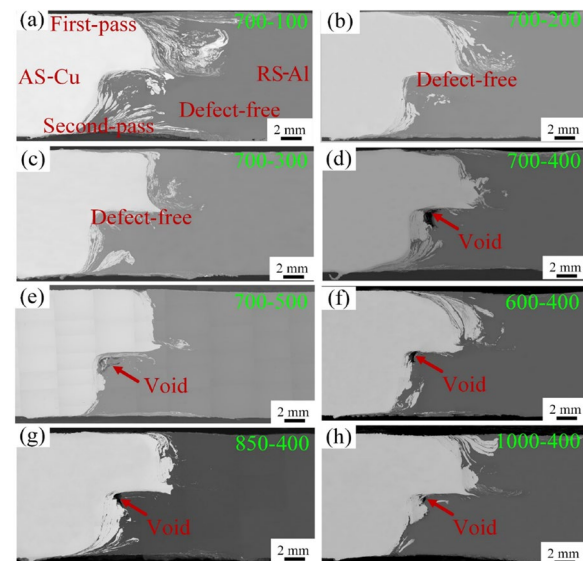
essentially free of plastic material sticking in the welding process, which causes better material flow and mixing, resulting in a defect-free and smooth welding surface.

Figure 5 displays the cross-sectional appearances of Al/Cu joints under different welding parameters, the rotational speed on both sides of Figure 5(a-e) is fixed at 700 r/min. When the welding speed is 100 mm/min, the extensive welding heat input causes many Cu blocks and Cu particles to enter the weld nugget zone (WNZ) and violently mix with Al. As the welding speed increases, the amount of Cu entering the stir zone begins to decrease gradually, Muthu et al. [18] also observed the same phenomenon. However, only a small amount of Cu is formed in the stir zone at 500 mm/min, which is mainly due to low welding heat input making the Cu near the Al/Cu interface difficult to detach from the Cu substrate. Furthermore, when the welding speed ranges from 100 to 300 mm/min, the joints are free of defects. And when

the welding speed is between 400 and 500 mm/min, the first-pass weld is defect-free, while void defects appear at the bottom of the second-pass weld. This is mainly due to the workpiece deformation caused by the first-pass weld, which leads to insufficient downforce during the second-pass welding process on the back of the workpiece. Taking the welding load of 700 r/min-400 mm/min as an example, the axial force and tool torque of both welds are illustrated in Figure 6. It is evident that the welding loads of the first-pass weld are higher than that of the second-pass weld during the tool travelling stage, this is because the workpiece appears to the slightly deformation after the joining of the first-pass weld on the front side of the workpiece, causing the tool shoulder is hard to tightly contact the surface of second-pass weld on the backside of the workpiece under the same plunge depth, thus the decrease occurs in the axial force and torque of the second-pass weld in comparison of first-pass weld. Figure 5 also depicts that the first-pass weld is defect-free, while void defects form at the bottom of the second-pass weld when the welding speed of both sides is fixed at 400 mm/min for different rotational speeds, which is also due to the insufficient downforce during the joining of second-pass weld. Moreover, with the increase of the rotational speed, the void defects of the second-pass weld become smaller and smaller. This is due to the fact that the increase of rotational speed improves welding heat input and material fluidity, which progressively reduces void defects of the second-pass weld.
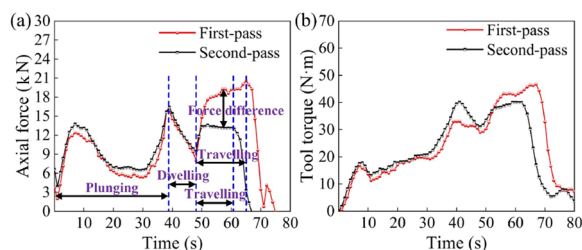
3.2 Interface Microstructure

For Al/Cu dissimilar materials, the generation of IMCs is inevitable, and the welding parameters primarily affect the IMCs layer thickness [23, 24]. Numerous studies have shown that a thicker IMCs layer will dramatically decrease joint's mechanical properties, while a thin IMCs layer is helpful to improve them [25–28].

Figure 7 shows the SEM morphology of the joint at seven typical positions (F1-F7) and the line scan results for the corresponding positions at the welding parameter

Figure 6 (**a**) Axial force and (**b**) tool torque of the joint at 700 r/min-400 mm/min

of 700 r/min-100 mm/min. Generally speaking, in the photograph of the SEM with the backscattered electron (BSE) mode, the colors of Al and Cu are represented as black and white, respectively. While the IMCs layer at the Al/Cu interface exhibits a grey color. According to the color difference, the Image J software is used to measure the thickness of IMCs at the Al/Cu interface. It illustrates that the weld is crack-free and forms a continuous IMCs layer. Figure 7(b-g) depicts that IMCs thickness gradually decreases from approximately 1.08 μm to 0.37 μm along the depth of the first-pass weld. According to the EDS point scan results of the first-pass weld (Table 1), the ratios of Al and Cu elements at points 2, 4 and 6 are approximately 2:1, which corresponds to possible IMCs of Al_2Cu. In addition, the content of Al and Cu elements at point 3 is approximately 4:9, which corresponds to possible IMCs of Al_4Cu_9. And the content of Al and Cu elements at points 1 and 5 are approximately equal to 2:3, and the corresponding IMCs are probably Al_2Cu_3. Figure 7(h) shows the microstructure in the middle of the lap surface, where some Cu blocks distributed in the stir zone. Owing to the low heat production of the pin during the DS-FSZW process, the IMCs layer at the lap surface is only approximately 0.23 μm, and the phase composition is probably Al_2Cu. Figure 7(j-p) corresponds to SEM images of the bottom, middle and top microstructures of the second-pass weld and the corresponding line scan images, respectively. According to Figure 7(j), a continuous and uniform IMCs layer of approximately 0.25 μm thick is formed at the bottom of the second-pass weld, where the phase composition is probably presumed as the Al_2Cu_3 and Al_2Cu based on the point scan result. The IMCs layer of Figure 7(m) is approximately 0.33 μm thick, the phase composition shows that the IMCs layer close to the Cu side (point 10) has an Al and Cu atom percentage of 36.9% and 63.1% respectively, indicating that Al_2Cu_3 may have been generated here. The IMCs layer close to the Al side (point 11) is probably Al_2Cu. Figure 7(o) depicts the IMC layer here is continuous but not uniform, with variations ranging from about 0.34 to 1.01 μm. This may be attributed to the fact that this area is close to the shoulder, where high welding heat input and violent material mixing contribute to a huge variation of the IMCs layer thickness. The point scan results indicate that the IMCs layer may consist of AlCu and Al_2Cu.

In summary, for the DS-FSZW joint at the welding parameter of 700 r/min-100 mm/min, a continuous IMCs layer without cracks is formed at the Al/Cu interface. At the same time, the IMCs layer at the top of the first-pass weld and the second-pass weld are not uniformly distributed, which may be caused by the intense mixing in this area due to excessive welding heat input and significant plastic deformation near the shoulder. What's more, it is
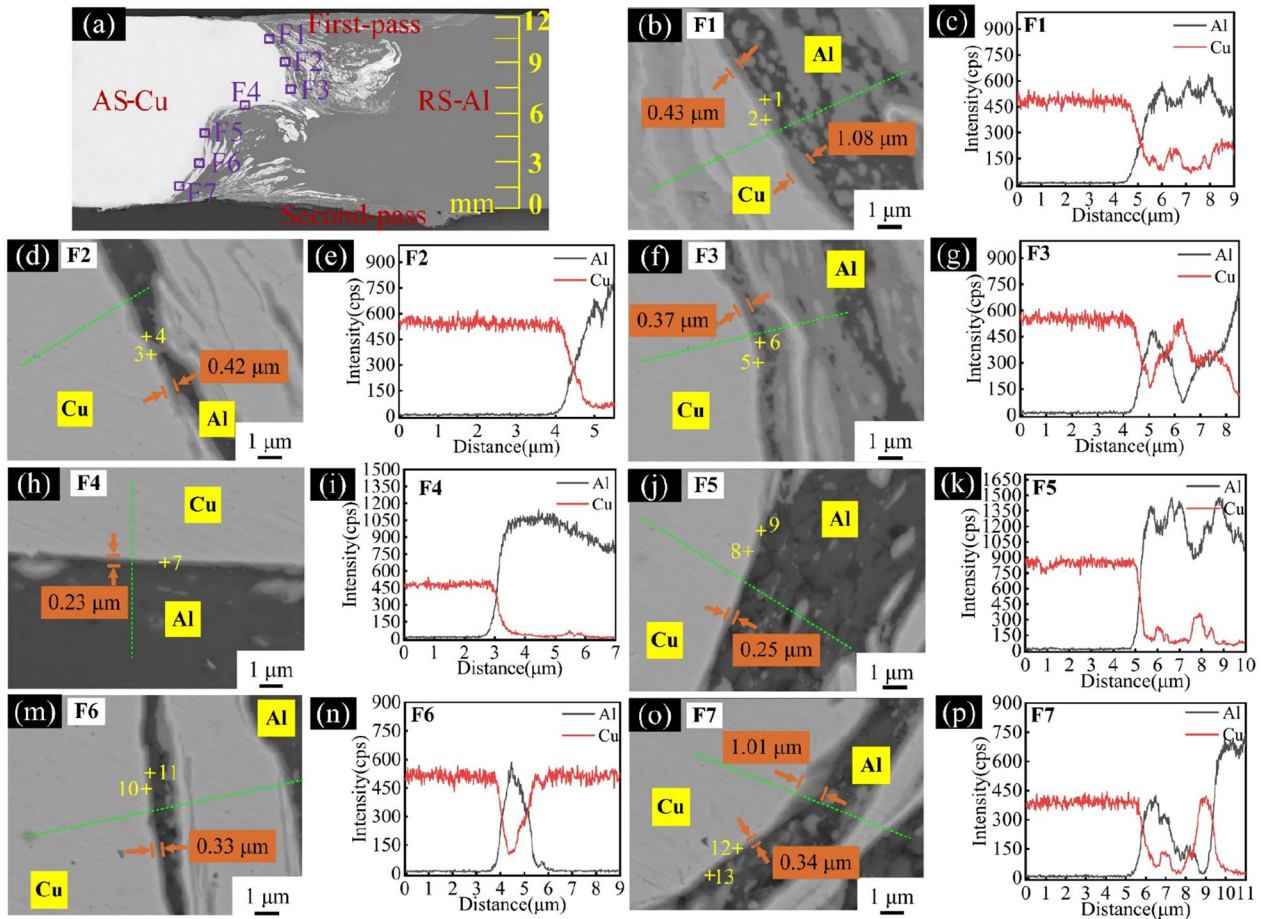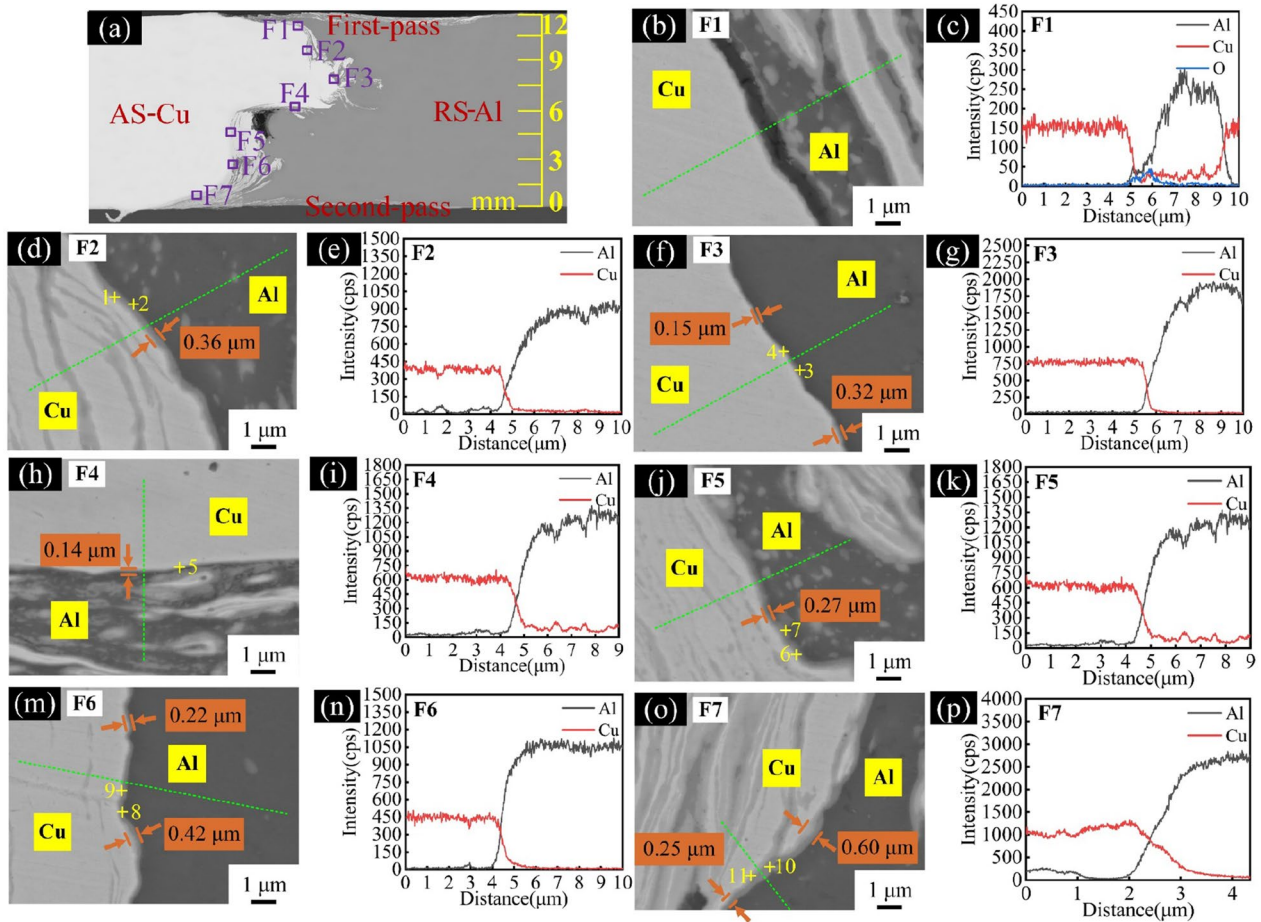
Figure 7 Microstructures and EDS lines at the Al/Cu interface of 700-100 joint: (**a**) The typical test positions for interfacial microstructure, (**b**)–(**p**) Corresponding SEM and EDS line scan results at locations F1-F7, respectively

Table 1 EDS point scan results and corresponding phase analysis for points marked in Figure 7

Point number	Al (at.%)	Cu (at.%)	Possible phases
1	44.3	55.7	Al_2Cu_3
2	65.9	34.1	Al_2Cu
3	27.8	72.2	Al_4Cu_9
4	69.1	30.9	Al_2Cu
5	45.2	54.8	Al_2Cu_3
6	67.3	32.7	Al_2Cu
7	68.3	31.7	Al_2Cu
8	45.2	54.8	Al_2Cu_3
9	67.3	32.7	Al_2Cu
10	36.9	63.1	Al_2Cu_3
11	69.9	30.1	Al_2Cu
12	51.8	48.2	$AlCu$
13	65.7	34.3	Al_2Cu

found that IMCs thickness decreases gradually from top to bottom for both welds.

Figure 8 shows the SEM morphology of the joint at seven typical positions (F1-F7) and the line scan results for the corresponding positions at 700 r/min-400 mm/min. Figure 8(b) shows that microcracks are found at the Al/Cu interface, the corresponding line scan also shows that the presence of cracks makes the oxygen content rise sharply at 6 μm from the start of the line scan (Figure 8(c)). Figure 8(d) depicts a continuous and uniform IMCs layer of approximately 0.36 μm thick is formed. Analysis of the EDS spot scan results indicates that the phase composition is Al_2Cu phase and α-Al+Al_2Cu. Figure 8(f) shows that the IMCs thickness formed ranges from approximately 0.15 to 0.32 μm. The composition analysis also indicates that the phases at this location are probably the Al_2Cu phase and α-Al+Al_2Cu. Figure 8(h) shows a large number of long Cu blocks and fine Cu particles, and the formation of IMCs layer is relatively

Figure 8 Microstructures and EDS lines at the Al/Cu interface of 700-400 joint: (**a**) The typical test positions for interfacial microstructure, (**b**)–(**p**) Corresponding SEM and EDS line scan results at locations F1-F7, respectively

flat. Based on the point scan results in Table 2, it is presumed that the phase composition in this area may be α-Al and Al_2Cu. Figure 8(j-p) shows SEM images and corresponding line scan images at different locations of the second-pass weld. Figure 8(j) shows that a continuous and uniform IMCs layer of approximately 0.27 μm thick is produced at the bottom of the second-pass weld, and the phase composition is presumed to be Al_2Cu and α-Al+Al_2Cu. Figure 8(m) illustrates that the IMCs layer is not uniformly distributed here and the thickness ranges from about 0.22 to 0.42 μm, the EDS spot scan identified that Al_2Cu and α-Al+Al_2Cu may have been generated here. Figure 8(o) also shows that the IMCs layer in this area is still continuous but not uniform, varying from approximately 0.25 to 0.60 μm, and Table 2 shows that the IMCs layer may consist of α-Al+Al_2Cu and AlCu.

Figure 9 shows the SEM morphology of the joint at seven typical positions (F1-F7) and the line scan results for the corresponding positions at 850 r/min-400 mm/min. Figure 9(b-g) shows the SEM images and

Table 2 EDS point scan results and corresponding phase analysis for points marked in Figure 8

| Point number	Al (at.%)	Cu (at.%)	Possible phases
1	67.4	32.6	Al_2Cu
2	79.8	20.2	α-Al+Al_2Cu
3	85.3	14.7	α-Al+Al_2Cu
4	63.6	36.4	Al_2Cu
5	73.9	26.1	α-Al+Al_2Cu
6	69.2	30.8	Al_2Cu
7	82.8	17.2	α-Al+Al_2Cu
8	80.7	19.3	α-Al+Al_2Cu
9	69.8	30.2	Al_2Cu
10	79.9	20.1	α-Al+Al_2Cu
11	50.3	49.7	AlCu
1	67.4	32.6	Al_2Cu
2	79.8	20.2	α-Al+Al_2Cu
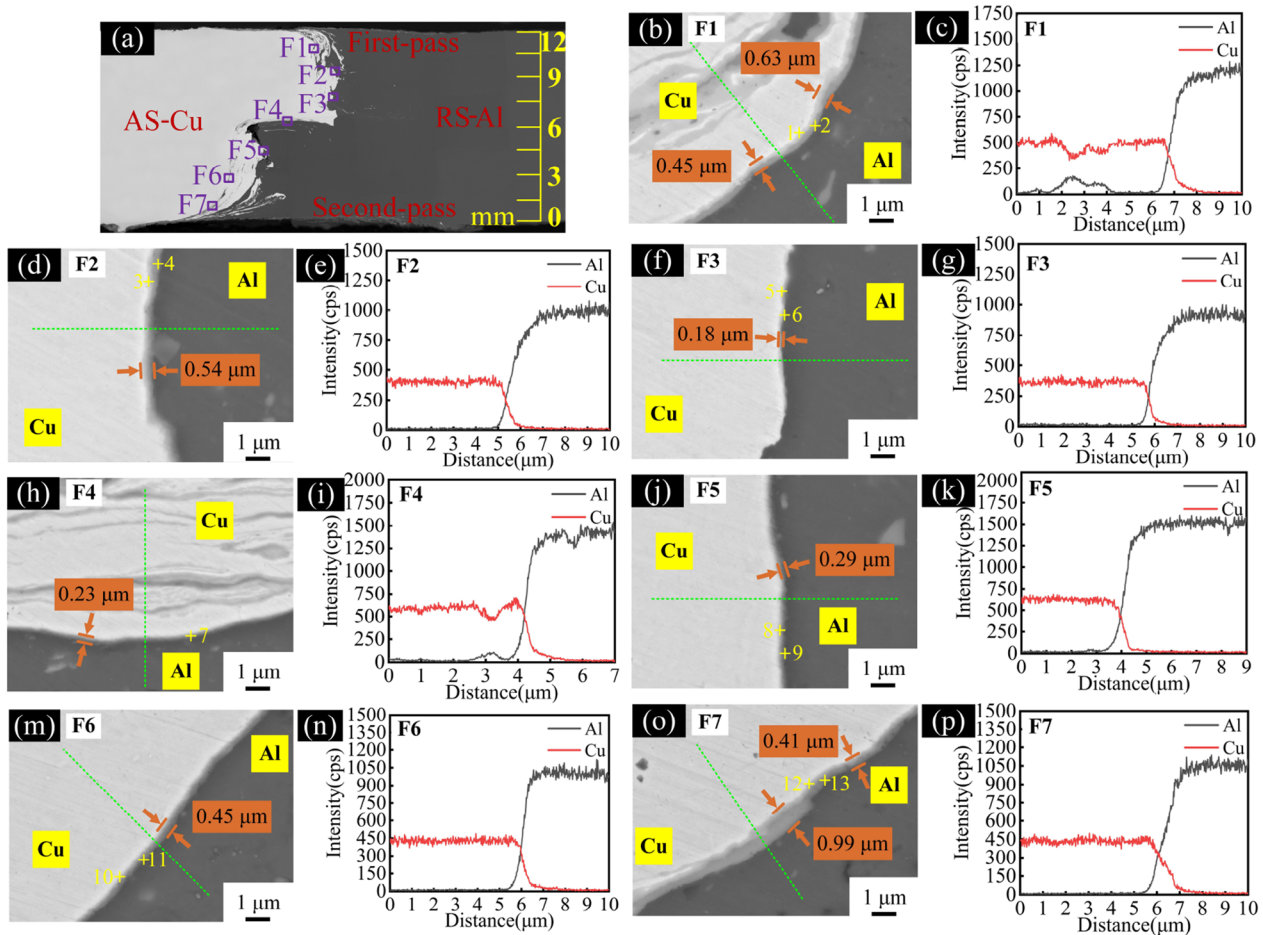
Figure 9 Microstructures and EDS lines at the Al/Cu interface of 850-400 joint: (**a**) The typical test positions for interfacial microstructure, (**b**)–(**p**) Corresponding SEM and EDS line scan results at locations F1-F7, respectively

corresponding line scan images of microstructure at different locations of the first-pass weld, as for Al/Cu interface, the thickest IMCs layer is approximately 0.63 μm and the smallest IMCs layer thickness is approximately 0.18 μm. Figure 9(d) depicts a continuous and uniform IMCs layer of approximately 0.54 μm thick is produced, the spot scan results in Table 3 suggest that the IMCs in the first-pass weld may consist of Al_2Cu and α-Al+Al_2Cu. Figure 9(h) shows microstructure in the middle of the lap surface, where the Al and Cu form a kind of curved interface, which is mainly attributed to the insertion of the pin into the Cu plate and its extrusion, the IMCs layer in this region is thin and no cracks are found. Figure 9(j-p) shows the SEM images and corresponding line scan images at different locations of second-pass weld. Figure 9(j) shows that a continuous and uniform IMCs layer of approximately 0.29 μm thick is produced, and the point scan results indicate that α-Al+Al_2Cu may have been generated at this location. Figure 9(m) shows that

Table 3 EDS point scan results and corresponding phase analysis for points marked in Figure 9

Point number	Al (at.%)	Cu (at.%)	Possible phases
1	79	21	Al_2Cu
2	85.7	14.3	α-Al+Al_2Cu
3	72.1	27.9	Al_2Cu
4	82.2	17.8	α-Al+Al_2Cu
5	68	32	Al_2Cu
6	81.2	18.8	α-Al+Al_2Cu
7	80.3	19.7	α-Al+Al_2Cu
8	84.4	15.6	α-Al+Al_2Cu
9	89.6	10.4	α-Al+Al_2Cu
10	73.8	26.2	Al_2Cu
11	89.2	10.8	α-Al+Al_2Cu
12	66.4	33.6	Al_2Cu
13	75.7	24.3	α-Al+Al_2Cu
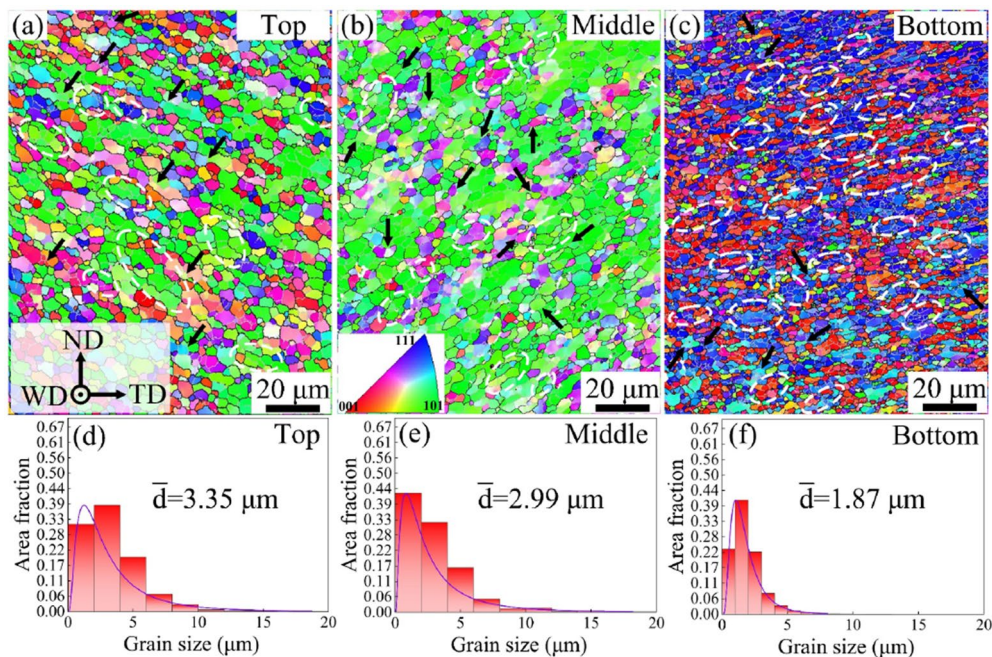
Figure 10 IPF map and grain size distribution at different locations in the WNZ of the first-pass weld for the welding condition of 850 r/min-400 mm/min: (**a**–**c**) IPF map, (**d**–**f**) Grain size distribution

the IMCs layer is approximately 0.45 μm thick here, and phase composition indicates that α-Al+Al$_2$Cu and Al$_2$Cu may have existed. Figure 9(o) depicts the IMCs layer here is non-uniform but continuous with variations ranging from approximately 0.41 to 0.99 μm and the IMCs layer probably consists of α-Al+Al$_2$Cu and Al$_2$Cu.

In summary, for the DS-FSZW joint under the welding parameter of 850 r/min-400 mm/min, a continuous IMCs layer with a thin thickness is formed on both sides. In addition, no cracks are found at the Al/Cu interface. Therefore, it is beneficial for the joint to obtain superior mechanical properties.

3.3 Microstructure in the Weld Nugget Zone
Dynamic recovery (DRV) and dynamic recrystallization (DRX) occur in the WNZ during the FSW process leading to grain refinement [29]. For the thermal-mechanical process, continuous dynamic recrystallization (CDRX) and geometric dynamic recrystallization (GDRX) are main dynamic recrystallization mechanisms of Al alloys. The severe plastic deformation and high peak welding temperatures during the DS-FSZW process create excellent conditions for dynamic recrystallization of the grains in WNZ.

Figure 10 shows the IPF map and grain size distribution in the Al side of WNZ of the first-pass weld under the welding condition of 850 r/min-400 mm/min, where the black grain boundaries are high-angle grain boundaries

(HAGBs, with the misorientation>15°) and the silver grey are low-angle grain boundaries (LAGBs, misorientation are in the range of 2° to 15°). Under the thermal-mechanical conditions of the DS-FSZW, dynamic recovery and dynamic recrystallization occur in the WNZ, so WNZ has both equiaxed grains and elongated grains. Figure 10(a) and (d) show the IPF map and grain distribution at the top of WNZ respectively, where the average grain size is approximately 3.35 μm, and the black arrows represent CDRX and the white circles represent GDRX. Furthermore, it can be seen from Figure 10(a) that the recrystallization mechanism belongs to CDRX and GDRX. Figure 10(b) and (e) show the IPF map and grain distribution in the middle of WNZ respectively. It can be found that the average grain size is about 2.99 μm and the recrystallization mechanism is also CDRX and GDRX. Figure 10(c) and (f) show the IPF map and grain distribution at the bottom of WNZ respectively, the statistical results reveal that the average grain size here is about 1.87 μm. It can be observed from the figure that most of the grains have jagged grain boundaries and there are many small grains inside the long strip of grains, which consistents with GDRX characteristics. At the same time, a small portion of the grains are surrounded by HAGBs and LAGBs segments, which indicates the grain occurring CDRX. Thus, the dominant mechanism for recrystallisation at the bottom of the WNZ is GDRX with partial CDRX. In terms of the statistical average grain size at
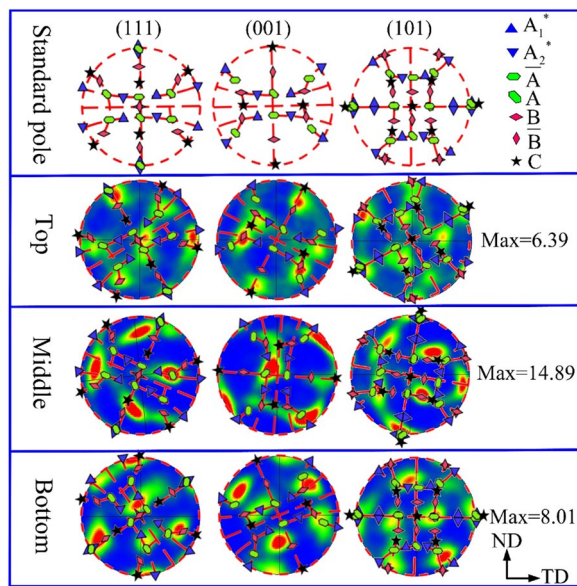
Figure 11 Standard pole figures and pole figures at different locations in the WNZ for the welding condition of 850 r/min-400 mm/min

different locations of the WNZ, the largest average grain size value is obtained at the top of the WNZ, while the smallest average grain size appears at the bottom of the WNZ, which is mainly due to the gradual decrease of the welding temperature from the top to bottom of WNZ. Furthermore, it also can be found that the orientation of the bottom of WNZ is mainly <111> direction, while the orientation of the top and middle of WNZ is mainly <101> orientation, and the grain orientation at the bottom of WNZ is greatly changed compared with the grain orientation of the top and middle of WNZ, which due to material flow direction and strain rate at the bottom of WNZ exists significant difference compared to the top and middle of WNZ, as well as the thermal cycling of the second-pass weld causing a large change in grain orientation at the bottom of WNZ.

As for the FSW process, the Al alloy is deformed by the tool to form a shear texture, and seven types of textures are formed during the deformation process, including $\{111\}<\overline{1}\overline{1}2>A_1^*$, $\{111\}<11\overline{2}>A_2^*$, $\{1\overline{1}1\}<110>A$, $\{\overline{1}\overline{1}\overline{1}\}<\overline{1}10>\overline{A}$, $\{1\overline{1}2\}<110>B$, $\{\overline{1}\overline{1}2\}<\overline{1}10>\overline{B}$, $\{001\}<110>C$ [30]. Figure 11 shows the standard polar map for face-centered cubic metal on (111), (001) and (101) crystallographic plane, as well as the polar map for the WNZ at the welding condition of 850 r/min-400 mm/min. It shows that the WNZ at the top is mainly composed of $B/\overline{B}$ and C textures, which indicates there exists a large shear strain at the top of the WNZ due to the influence of the shoulder which results in the strong texture of $B/\overline{B}$ and C [30, 31]. The middle of WNZ is mainly

composed of C and A_1^*/A_2^* textures, and the bottom of WNZ is mainly composed of A_1^*/A_2^* and $A/\overline{A}$ type textures, which indicates that the bottom of WNZ experiences a small shear strain [32]. This is due to the bottom of WNZ being mainly affected by the pin, which experiences a low shear strain. By comparing the texture at different locations of WNZ, it depicted that the types of texture are various. Furthermore, the texture strength at the top, middle and bottom of WNZ of the first-pass weld is 6.39 MRD, 14.89 MRD and 8.01 MRD respectively. Since the preferential orientation of WNZ at the top is not evident, the middle and bottom of WNZ have obvious preferential orientation. Thus, the texture strength at the top of WNZ is lower than the texture strength in the middle and bottom of WNZ.

3.4 Mechanical Properties

Figure 12 shows the microhardness distribution at the typical positions of the joint under different welding parameters, the microhardness is measured at different depths of the joint, as shown the Figure 12(a) and (b) shows a large number of microhardness values within the WNZ under the 700 r/min-100 mm/min, which are higher than the Cu and Al substrates, it may be associated with the production of hard and brittle IMC in WNZ [33, 34]. The HAZ on both the Al side and Cu side shows a certain degree of softening, which results in a lower hardness value, especially on the Al side where the softening effect is very obvious. Meanwhile, in the HAZ of the Al alloy, the top of the joint has the lowest hardness, while the middle of the joint has a higher hardness than the top of the joint, which is mainly caused by the coarsening of the grains due to the higher temperature at the top of the joint. And the temperature of the middle of the joint is lower compared to top of the joint, which effectively inhibits the growth of the grains, and the hardness of the middle of the joint is relatively high. Furthermore, it is clear that as the welding speed increases, the high microhardness of the WNZ decreases. And the joint produced at the welding condition of 850 r/min-400 mm/min (Figure 12(d)) displays the most homogenous microhardness distribution in the WNZ.

Figure 13(a) demonstrates the mechanical properties of DS-FSZW joints under different welding speed conditions (the rotational speed is fixed at 700 mm/min), when the welding speed is 400 mm/min, the joint's tensile strength reaches a peak of 157.13 MPa, which is approximately 64.13% of Cu alloy and the elongation is 7.22%. As for lower welding speeds, such as 100 mm/min, despite the joint is free of void defects, the large welding heat input generates many IMCs, which seriously decreases the joint strength. Although tiny void defects exist at a welding speed of 400 mm/min, a continuous and thin
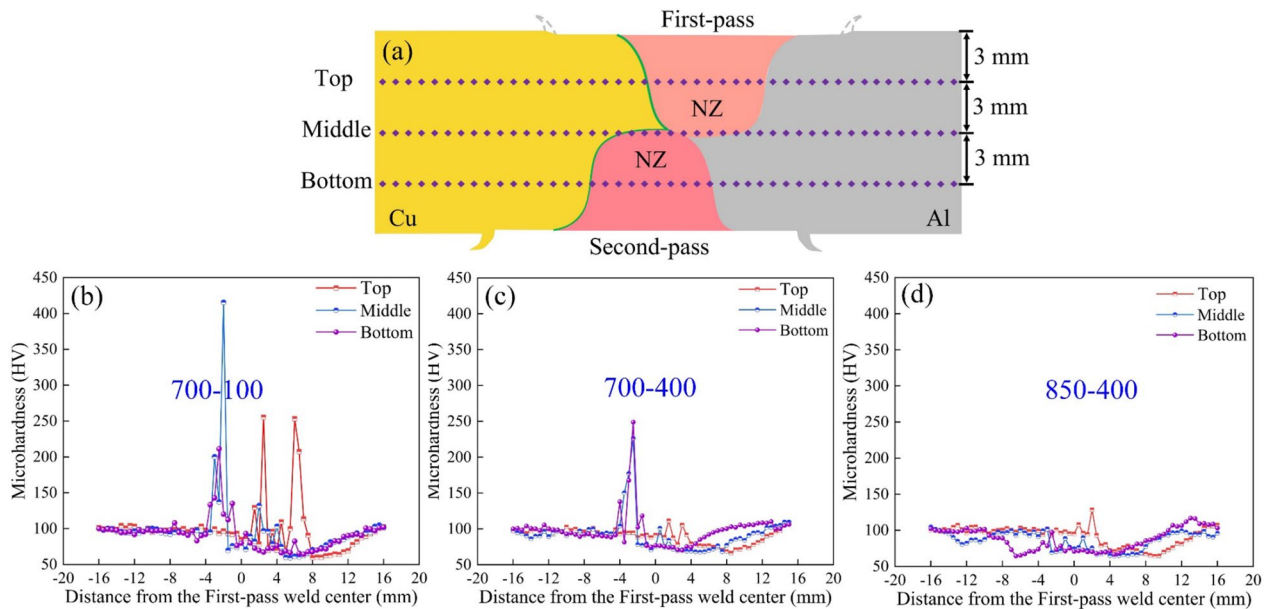
Figure 12 Microhardness distribution at different welding parameters: (**a**) Schematic of tested positions for microhardness test, (**b**) 700-100, (**c**) 700-400, (**d**) 850-400
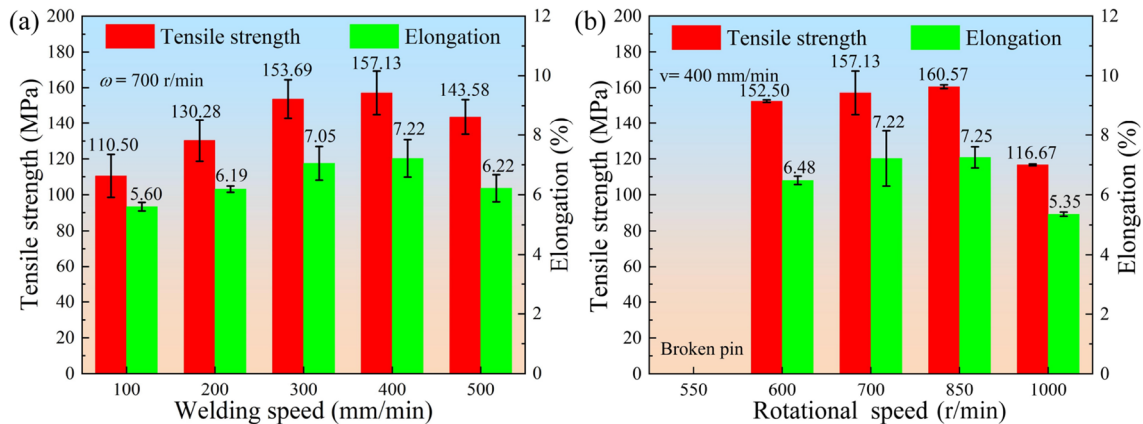
Figure 13 Tensile properties of DS-FSZW joint: (**a**) Different welding speed, (**b**) Different rotational speed

IMCs layer is generated at the Al/Cu interface causing a low internal stress and deformation, which effectively improves the joint's tensile properties. Larger void defects are formed because of the high welding speed and the insufficient downforce for the second-pass welding process at the welding speed of 500 mm/min, which weakens the joint's tensile strength. Figure 13(b) demonstrates the tensile properties of DS-FSZW joint under different rotational speed conditions (the welding speed is fixed at 400 min). It demonstrates that the joint's tensile strength shows a tendency to initially increase and then decrease with an increasing rotational speed. The joint's tensile strength reaches a peak of 160.57 MPa at

850 r/min, which is approximately 65.54% of the Cu substrate, and the elongation of the joint is 7.25%. The low rotational speed of 550 r/min produces a small welding heat input, which cannot soften the Al and Cu substrate in time, resulting in the pin being exposed to a large forward resistance during the welding process. Thus, the pin made of H13 steel is broken at the low rotational speed. In the range of 600–850 r/min, the joint's tensile strength tends to increase with an increasing speed and the increase in strength is not significant and fluctuates within 10 MPa, the optimum tensile strength of the joint is obtained at 850 r/min. However, the mechanical

properties of the joint decrease dramatically at 1000 r/min due to the formation of the thick IMCs layer.

3.5 Corrosion Behaviour

Figure 14 shows the polarization curve of base materials (i.e., Al alloy and T2 Cu), as well as the polarization curve of the joints achieved at different welding conditions. The Tafel extrapolation method can be obtained from the electrochemical corrosion of two important parameters, namely corrosion potential and corrosion current density. A higher corrosion potential indicates a lower corrosion tendency, while the corrosion potential cannot be applied to fully identify the material's corrosion resistance [35]. Corrosion current density is used to evaluate the material's corrosion rate. When the corrosion current density is higher, the material's corrosion resistance is worse, and corrosion resistance can be better reflected by the corrosion current density [36]. Table 4 gives the specific corrosion potential and corrosion current density values of the base metal and welded joints, the corrosion current density is ranked from small to large in order: Cu-base metal < Al-base metal < 850-400 joint < 700-400 joint < 700-100 joint < 1000-400 joint.

Since the corrosion current density of the Al/Cu base material is much lower than that of the welded joints, the corrosion resistance of the welded joints is worse than that of the base material. It indicates that the metallurgical reactions occur in the Al/Cu interface, which weakens the material's corrosion resistance. This is mainly because of the potential difference between Al and Cu. Specifically, the low-potential Al alloy will act as the cathode and the high-potential Cu as the anode, forming a galvanic corrosion primary battery in the 3.5 wt% NaCl electrolyte solution. Moreover, the potential of IMCs such as Al_2Cu and Al_4Cu_9 is also not consistent with Al and Cu, so there is still a potential difference between different phases forming micro-area primary batteries between IMCs and Cu, or IMCs and Al. It will

Table 4 Corrosion potential and corrosion current density of base metal and welded joints

Parameter	E_{corr} (V_{SCE})	i_{corr} ($A \cdot cm^{-2}$)
Al-base metal	− 0.707	6.73×10^{-6}
Cu-base metal	− 0.216	4.842×10^{-8}
700–100	− 0.676	6.457×10^{-5}
700–400	− 0.687	3.793×10^{-5}
850–400	− 0.686	3.741×10^{-5}
1000–400	− 0.675	8.185×10^{-5}

accelerate the corrosion of welded joints when IMCs are excessive.

For all the welded joints, the joint at the welding parameter of 850 r/min-400 mm/min has the highest corrosion resistance. The reason can probably be attributed to two sides. On the one hand, according to the investigation of Ma et al. [37], the un-welded defect in the Al/steel dissimilar joint enlarged contact areas between the Al/Cu matrix and corrosive solution when the joint was immersed into the solution, contributing to a faster dissolution of Al at the interface, thus the corrosion resistance of joint became poor. Since Al/Cu joints under the parameter of 850-400 have small void defects, it can effectively inhibit the deterioration of the corrosion performance of the joints. On the other hand, the thickness of the IMCs layer also plays an important role in the joint's corrosion property. Pan et al. [38] studied the corrosion property of Al/steel resistant spot welding (RSW) joint, the results revealed that the IMC phases produced the local potential differences contributing to localized galvanic corrosion between the Al and IMCs. The formation of the thicker IMCs at the Al/steel interface accelerated the corrosion of Al. Thus the corrosion resistance of the Al/Steel joint was reduced. Sravanthi [39] reported that the thickness of the IMCs layer increases as the welding speed decreases. A thicker IMC layer caused
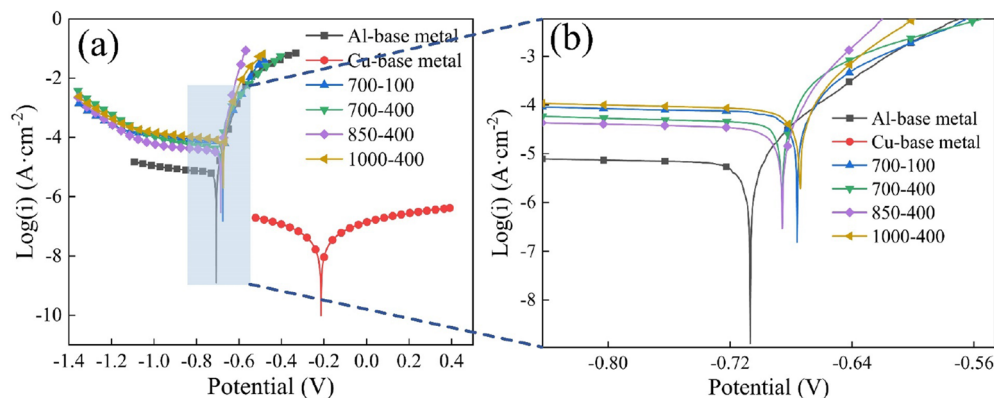
**Figure 14** (**a**) Polarization curve, (**b**) An enlarged view of region marked in (**a**)
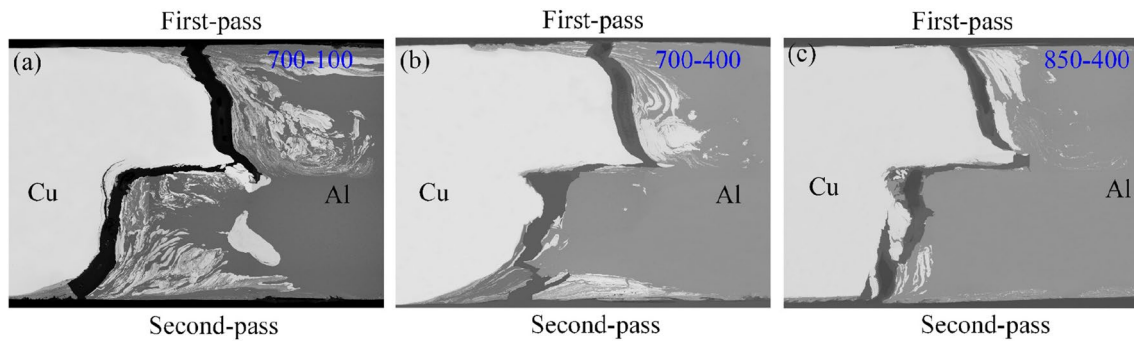
Figure 15 Fracture locations of Al/Cu DS-FSZW joints at different welding parameters: (**a**) 700-100, (**b**) 700-400, (**c**) 850-400

more severe corrosion at the interface of the joint. And the Al/Cu dissimilar joint on the condition of 850-400 has a thinner IMCs layer, thus it is beneficial to improve the corrosion property of the joint. Therefore, Al/Cu dissimilar joint at the parameter of 850-400 achieved a superior corrosion performance in this paper which may attributed to the the smaller void defects and the formation of a thinner IMCs layer. And by combining the aforementioned test results of the joint's tensile properties, the maximum tensile strength is also obtained with the 850 r/min-400 mm/min parameter, which indicates that the welded joint can maintain a high level of corrosion performance as well as maintaining a high tensile strength, the phenomenon also observed in Al/steel joints by Ma et al. [37].

3.6 Failure Mechanism

Figure 15 shows the fracture locations of Al/Cu joints at different welding parameters. From Figure 15(a), it can be observed that some Al alloy sticks to the top of both welds for the welding condition of 700 r/min-100 mm/min, but the joint's majority fracture occurs at the Al/Cu interface. Figure 15(b) shows the fracture location at 700 r/min-400 mm/min, where most of the Al alloy still adheres at the top of both welds and the fracture occurs in the WNZ, indicating that the Al/Cu interface at the top of both welds is not the weakest zone. In contrast, beyond the top of both welds, fracture occurs essentially at the Al/Cu interface, which is mainly due to the existence of hard and brittle IMCs in this area, and cracks tend to initiate and propagate at the location of IMCs layer. Eventually the joint fractures at the Al/Cu interface. Figure 15(c) shows the joint's fracture location at 850 r/min-400 mm/min, the fracture location at this condition is along the Al/Cu interface, which indicates that the Al/Cu interface is still the weakest zone of the joint, this is also because the IMCs are produced at interface, cracks will easily initiate and propagate at interface during the
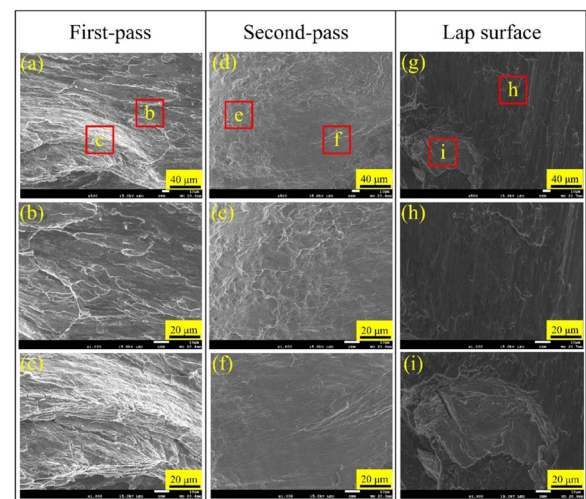
Figure 16 SEM images of fracture morphologies of the Al side at the welding condition of 700 r/min-100 mm/min: (**a**–**c**) First-pass weld, (**d**–**f**) Second-pass weld, (**g**–**i**) Lap surface
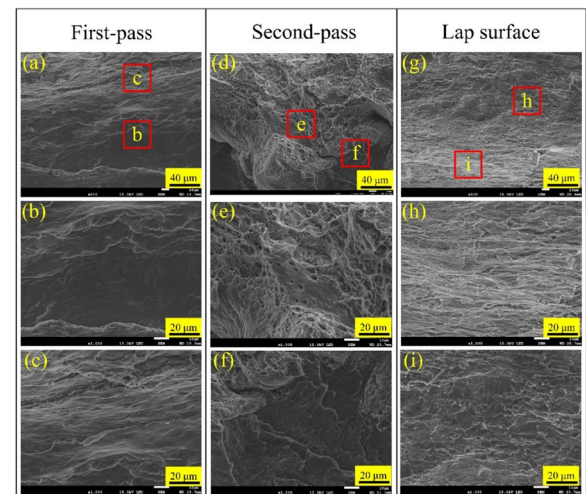
Figure 17 SEM images of fracture morphologies of the Al side at the welding condition of 700 r/min-400 mm/min: (**a**–**c**) First-pass weld, (**d**–**f**) Second-pass weld, (**g**–**i**) Lap surface

tensile test, and the joint finally fractures at the Al/Cu interface.

Figures 16, 17 and 18 show the fracture morphology of the Al side of the DS-FSZW joint at 700 r/min-100 mm/min, 700 r/min-400 mm/min and 850 r/min-400 mm/min respectively. Figure 16 shows that cleavage planes and tearing ridges exist on the fracture surface for both welds, which implies the joint undergoes brittle fracture, this is mainly due to the lower welding speed under this parameter causing a large welding heat input, so the crack is easily initiated and propagated from the thick IMCs layer of the Al/Cu interface, finally the joint exhibits a brittle fracture mode. Figure 17 shows cleavage planes and tearing ridge characteristics because top interface of the first-pass weld has microcracks, so cracks tend to expand from this area during the tensile test and the first-pass weld is quickly fractured under the tensile force. In terms of the second-pass weld, it reveals that the tensile fracture of the second-pass weld is distributed with cleavage planes and dimples with various sizes, owing to the formation of a continuous and thin IMCs layer at the Al/Cu interface of the second-pass weld, which effectively suppresses crack initiation and propagation, thus the joint represents a mixed ductile-brittle fracture under the welding condition of 700 r/min-400 mm/min. Figure 18 shows the fracture morphology of the DS-FSZW joint at 850 r/min-400 mm/min. There are very dense and small dimples distributed on the fracture surface of the first-pass weld as well as tearing ridges and cleavage planes. Therefore, the first-pass weld is fractured in a mixed ductile-brittle fracture. The second-pass weld is also a mixed ductile-brittle fracture because of the

presence of large dimples and cleavage planes. For the lap surface, the fracture morphology shows a river pattern with no obvious dimple structure. Thus, the joint shows a mixed ductile-brittle fracture under the welding condition of 850 r/min-400 mm/min.

4 Conclusions

A novel DS-FSZW method has been employed to join medium-thick 6061-T6 Al alloy and T2 pure Cu. The influence of welding parameters on microstructure, corrosion behaviour and mechanical properties has been systematically studied and the conclusions can be summarised as follows:

(1) In the DS-FSZW, the void defects are easily produced in the second-pass weld. This is due to the weld distortion that occurs after the completion of the first-pass weld, which causes a lower downforce at the welding process of the second-pass weld under the same plunge depth, and the first-pass weld may crack if improper welding parameters are applied in the DS-FSZW.

(2) The recrystallisation mechanisms for the top and middle grains of the WNZ for the DS-FSZW joints are CDRX and GDRX, while the dominant recrystallization mechanism at the bottom of the WNZ of the first-pass weld is GDRX with partial CDRX. The average grain size decreases from the top to the bottom of the WNZ due to the gradual decrease in welding temperature.

(3) The top of the WNZ for DS-FSZW joints experiences a larger shear strain which results in a texture of $B/\overline{B}$ and C textures. While the bottom of the WNZ experiences a smaller strain, this leads to formation of A_1^*/A_2^* type textures.

(4) A continuous thin layer of IMCs was achieved in the Al/Cu DS-FSZW joint at 850 r/min-400 mm/min. The joint has a maximum tensile strength of 160.57 MPa, reaching 65.54% of the pure Cu substrate. The fracture of the joint occurs at the Al/Cu interface with a mixed ductile-brittle fracture.

(5) The corrosion resistance of the Al/Cu DS-FSZW joint is lower than that of the base materials. The corrosion resistance of the joint is optimal under the welding condition of 850 r/min-400 mm/min. It indicates that the DS-FSZW process can achieve reliable Al/Cu joints with excellent mechanical properties and corrosion resistance.
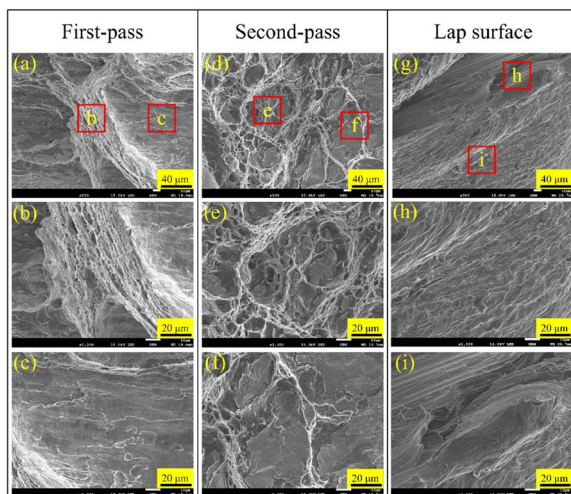
Figure 18 SEM images of fracture morphologies of the Al side at the welding condition of 850 r/min-400 mm/min: (**a**–**c**) First-pass weld, (**d**–**f**) Second-pass weld, (**g**–**i**) Lap surface

Declarations

Competing Interests

The authors declare that they have no conflict of interest.

References

[1] G Li, J Song, X Lu, et al. Investigation on microstructure and mechanical properties of Al/Cu butt joints by CMT method in asymmetrical V-groove configuration. *Metallurgical Research & Technology*, 2020, 117 (3): 303-314.

[2] X Zhou, G Zhang, Y Shi, et al. Microstructures and mechanical behaviour of Al-Cu lap joints. *Materials Science and Engineering: A*, 2017, 705: 105-113.

[3] F Cai, L Zhang, Y Li, et al. Study on microstructure and mechanical properties of Cu/Al joints brazed by flux-cored Al-Si filler metal. *Vacuum*, 2022, 201: 111066.

[4] F Ji, S B Xue, J Y Lou, et al. Microstructure and properties of Cu/Al joints brazed with Zn-Al filler metals. *Transactions of Nonferrous Metals Society of China*, 2012, 22(2): 281-287.

[5] Z Shen, Y Ding, W Guo, et al. Refill friction stir spot welding Al alloy to Cu via pure metallurgical joining mechanism. *Chinese Journal of Mechanical Engineering*, 2021, 34: 75.

[6] S Ji, Z Li. Microstructure and mechanical properties of friction stir lap welded Mg/Al joint assisted by stationary shoulder. *Metals and Materials International*, 2017, 23: 1158-1167.

[7] M Geyer, V Vidal, T Pottier, et al. Investigations on the material flow and the role of the resulting hooks on the mechanical behaviour of dissimilar friction stir welded Al2024-T3 to Ti-6Al-4V overlap joints. *Journal of Materials Processing Technology*, 2021, 292: 117057.

[8] B Seo, K H Song, K Park. Corrosion properties of dissimilar friction stir welded 6061 aluminum and HT590 steel. *Metals and Materials International*, 2018, 24: 1232-1240.

[9] H J Zhang, H J Liu, J L Song, et al. Influence of tool offset on performance of thin Al-Cu dissimilar metal friction stir butt welded joint. *Transactions of the Indian Institute of Metals*, 2020, 73: 2549-2559.

[10] R Khajeh, H R Jafarian, S H Seyedein, et al. Microstructure, mechanical and electrical properties of dissimilar friction stir welded 2024 Al alloy and Cu joints. *Journal of Materials Research and Technology*, 2021, 14: 1945-1957.

[11] N A Muhammad, C S Wu. Evaluation of capabilities of ultrasonic vibration on the surface, electrical and mechanical behaviours of Al to Cu dissimilar friction stir welds. *International Journal of Mechanical Sciences*, 2020, 183: 105784.

[12] J You, Y Zhao, C Dong, et al. Improving the microstructure and mechanical properties of Al/Cu dissimilar joints by ultrasonic dynamic-stationary shoulder friction stir welding. *Journal of Materials Processing Technology*, 2023, 311: 117812.

[13] W j Wang, H Wang, X f Liu, et al. Interface evolution and strengthening of two-step roll bonded Cu/Al clad composites. *Materials Characterization*, 2023, 199: 112778

[14] S Yan, Z Li, L. Song, et al. Research and development status of laser micro-welding of Al-Cu dissimilar metals: A review. *Optics and Lasers in Engineering*, 2023, 161: 107312.

[15] K Wang, S L Shang, Y Wang, et al. Unveiling non-equilibrium metallurgical phases in dissimilar Al/Cu joints processed by vaporizing foil actuator welding. *Materials & Design*, 2020, 186: 108306.

[16] S V Safi, H Amirabadi, M K B Givi, et al. The effect of preheating on mechanical properties of friction stir welded dissimilar joints of pure Cu and AA7075 Al alloy sheets. *The International Journal of Advanced Manufacturing Technology*, 2016, 84: 2401-2411.

[17] M N Avettand-Fenoël, R Taillard, G Ji, et al. Multiscale Study of Interfacial Intermetallic Compounds in a Dissimilar Al 6082-T6/Cu Friction-Stir Weld. *Metallurgical and Materials Transactions A*, 2012, 43: 4655-4666.

[18] M F X Muthu, V Jayabalan. Tool travel speed effects on the microstructure of friction stir welded Al-Cu joints. *Journal of Materials Processing Technology*, 2015, 217: 105-113.

[19] K P Mehta, V J Badheka. Effects of tilt angle on the properties of dissimilar friction stir welding Cu to Al. *Materials and Manufacturing Processes*, 2016, 31(3): 255-263.

[20] J Ouyang, E Yarrapareddy, R Kovacevic. Microstructural evolution in the friction stir welded 6061 Al alloy (T6-temper condition) to Cu. *Journal of Materials Processing Technology*, 2006, 172(1): 110-122.

[21] J X Tang, L Shi, C S Wu, et al. Microstructure and mechanical properties of dissimilar double-side friction stir welds between medium-thick 6061-T6 Al and pure Cu plates. *Acta Metallurgica Sinica (English Letters)*, 2022, 35(12): 2027-2046.

[22] J X Tang, L Shi, C S Wu, et al. Development of novel double-side friction stir Z shape butt-lap welding process for dissimilar joining of 12 mm medium-thick Al/Cu plates. *Materials Letters*, 2023, 331: 133445.

[23] J You, Y Zhao, C Dong, et al. Microstructural evolution and mechanical properties of the Al/Cu dissimilar joint enhanced by stationary-dynamic shoulder friction stir welding. *Journal of Materials Processing Technology*, 2022, 300: 117402.

[24] W Hou, L H Ahmad Shah, G Huang, et al. The role of tool offset on the microstructure and mechanical properties of Al/Cu friction stir welded joints. *Journal of Alloys and Compounds*, 2020, 825: 154045.

[25] P Xue, B L Xiao, D R Ni, et al. Enhanced mechanical properties of friction stir welded dissimilar Al/Cu joint by intermetallic compounds. *Materials Science and Engineering: A*, 2010, 527(21-22): 5723-5727.

[26] Y Mao, Y Ni, X Xiao, et al. Microstructural characterization and mechanical properties of micro friction stir welded dissimilar Al/Cu ultra-thin sheets. *Journal of Manufacturing Processes*, 2020, 60: 356-365.

[27] X Fei, Y Ye, L Jin, et al. Special welding parameters study on Cu/Al joint in laser-heated friction stir welding. *Journal of Materials Processing Technology*, 2018, 256: 160-171.

[28] S K Lader, M Baruah, R Ballav. Significance of underwater friction stir welding on the weld integrity of thin sheets of Al (AA1050-O) and brass (CuZn34) joints. *Materials Science and Engineering: A*, 2023, 865: 144627.

[29] Z Y Ma, R S Mishra, M W Mahoney. Superplastic deformation behaviour of friction stir processed 7075Al alloy. *Acta Materialia*, 2002, 50(17): 4419-4430.

[30] R W Fonda, J F Bingert. Texture variations in an Al friction stir weld. *Scripta Materialia*, 2007, 57(11): 1052-1055.

[31] R W Fonda, K E Knipling. Texture development in friction stir welds. *Science and Technology of Welding and Joining*, 2011, 16(4): 288-294.

[32] A Garg, A Bhattacharya. Effect of microstructural variation on strain localization in double-sided friction stir welded AA6061-AA7075 joints. *Strain*, 2022, 58(4): e12413.

[33] Y Mao, D Qin, X Xiao, et al. Achievement of high-strength Al/Cu dissimilar joint during submerged friction stir welding and its regulation mechanism of intermetallic compounds layer. *Materials Science and Engineering: A*, 2023, 865: 144164.

[34] M Zhang, Y D Wang, P Xue, et al. High-quality dissimilar friction stir welding of Al to steel with no contacting between tool and steel plate, *Materials Characterization,* 2022, 191: 112128.

[35] C Liu, Y Gao, K Chong, et al. Effect of Nb content on the microstructure and corrosion resistance of FeCoCrNiNbx high-entropy alloys in chloride ion environment. *Journal of Alloys and Compounds*, 2023, 935: 168013.

[36] H Ma, G Qin, P Geng, et al. Effect of intermetallic compounds on the mechanical property and corrosion behaviour of Al alloy/steel hybrid fusion-brazed welded structure. *Journal of Manufacturing Processes*, 2022, 75: 170-180.

[37] H Ma, G Qin, P Geng, et al. Microstructural characterisation and corrosion behaviour of Al alloy/steel hybrid structure produced by friction welding. *Journal of Manufacturing Processes*, 2021, 61: 349-356.

[38] B Pan, H Sun, D Xie, et al. Influence of accelerated corrosion on Al/steel RSW joints by in situ compression tests. *Materials Science and Engineering: A*, 2024, 889: 145851.

[39] S S Sravanthi, S G Acharyya, K V Phani Prabhakar, et al. Effect of welding parameters on the corrosion behavior of dissimilar alloy welds of T6 AA6061 Al-Galvanized mild steel. *Journal of Materials Engineering and Performance*, 2018, 27: 5518-5531.

Jiuxing Tang is currently a research assistant at *Department of Industrial and Systems Engineering, The Hong Kong Polytechnic University, Hong Kong, China*. He received his master degree from *Shandong University, China*, in 2023. His research interests include friction stir welding of dissimilar materials and sustainable ultra-precision machining of titanium alloy.

Guoxin Dai is a doctoral student at *School of Materials Science and Engineering, Shandong University, China*. His research interests include friction stir welding of lightweight materials.

Lei Shi is currently a professor at *School of Materials Science and Engineering, Shandong University, China*. He received his doctoral degree from *Shandong University, China*, in 2016. His research interests include friction stir welding and additive manufacturing.

Chuansong Wu currently works at *Institute of Materials Joining, Shandong University, China*. He is the Fellow of *American Welding Society*, and Humboldtian Scholar in Germany. His research interests include the physics of welding, numerical simulation and experimental sensing & control of various welding processes.

Sergey Mironov is currently a professor at *Laboratory of Mechanical Properties of Nanoscale Materials and Superalloys, Belgorod State University, Russia*. He received his doctoral degree from *Institute for Metals Superplasticity Problems, Russia*, in 2016. His research interests include friction stir welding and welding metallurgy.

Surendra Kumar Patel is currently a post-doc researcher at *Institute of Materials Joining, Shandong University, China*. He received his doctoral degree from *National Institute of Technology Mizoram, India*, in 2022. His research interests include friction stir processing and welding.

Song Gao is currently a lecturer *School of Mechanical Engineering, Qilu University of Technology (Shandong Academy of Sciences), China*. He received his doctoral degree from *Shandong University, China*, in 2018. His research interests include friction stir welding.

Mingxiao Wu is currently a senior engineer at *State Grid Henan Electric Power Research Institute, China*. He received his master degree from *Shandong University, China*, in 2017. His research interests include welding and joining technology in power transmission and transformation industry.